▌ Electrocatalysis

# Factors Governing the Activity of α-MnO$_2$ Catalysts in the Oxygen Evolution Reaction: Conductivity versus Exposed Surface Area of Cryptomelane

Justus Heese-Gärtlein,[a] Dulce M. Morales,[b] Anna Rabe,[a] Thomas Bredow,[c] Wolfgang Schuhmann,[b] and Malte Behrens*[a, d]

**Abstract:** Cryptomelane (α-(K)MnO$_2$) powders were synthesized by different methods leading to only slight differences in their bulk crystal structure and chemical composition, while the BET surface area and the crystallite size differed significantly. Their performance in the oxygen evolution reaction (OER) covered a wide range and their sequence of increasing activity differed when electrocatalysis in alkaline electrolyte and chemical water oxidation using Ce$^{4+}$ were compared. The decisive factors that explain this difference were identified in the catalysts' microstructure. Chemical water oxidation activity is substantially governed by the exposed surface area, while the electrocatalytic activity is determined largely by the electric conductivity, which was found to correlate with the particle morphology in terms of needle length and aspect ratio in this sample series. This correlation is rather explained by an improved conductivity due to longer needles than by structure sensitivity as was supported by reference experiments using H$_2$O$_2$ decomposition and carbon black as additive. The most active catalyst R-cryptomelane reached a current density of 10 mA cm$^{-2}$ at a potential 1.73 V without, and at 1.71 V in the presence of carbon black. The improvement was significantly higher for the catalyst with lower initial activity. However, the materials showed a disappointing catalytic stability during alkaline electrochemical OER, whereas the crystal structure was found to be stable at working conditions.

[a] Dr. J. Heese-Gärtlein, A. Rabe, Prof. Dr. M. Behrens
Faculty of Chemistry and
Center for Nanointegration Duisburg-Essen (CENIDE)
University of Duisburg-Essen
Universitätsstr. 7, 45114 Essen (Germany)
E-mail: malte.behrens@uni-due.de

[b] Dr. D. M. Morales, Prof. Dr. W. Schuhmann
Analytical Chemistry—Center for Electrochemical Sciences (CES)
Faculty of Chemistry and Biochemistry, Ruhr University Bochum
Universitätsstr. 150; 44780 Bochum (Germany)

[c] Prof. Dr. T. Bredow
Mulliken Center for Theoretical Chemistry
Institut für Physikalische und Theoretische Chemie
University of Bonn
Beringstr. 4; 53115 Bonn (Germany)

[d] Prof. Dr. M. Behrens
Ertl Center for Electrochemistry and Catalysis
Gwangju Institute of Science (GIST)
123 Cheomdan-gwagiro (Oryang-dong), Buk-gu
Gwangju 500-712 (South Korea)

📱 Supporting information and the ORCID identification number(s) for the author(s) of this article can be found under:
https://doi.org/10.1002/chem.201905090.

## Introduction

Manganese oxides receive considerable attention as potential water oxidation catalysts and have been studied for the oxygen evolution reaction (OER) electrochemically as well as in presence of sacrificial oxidants.[1] In comparison with other transition metal oxides such as nickel or cobalt oxides, pure manganese oxides or (oxy)hydroxides were commonly observed to be less active OER catalysts,[2] but further work is motivated by the high abundance and low toxicity of manganese compounds and/or inspired by the presence of manganese in water oxidation cluster in nature's photosystem II. In comparative studies, a large range of activities has been observed for different manganese oxide catalysts. Aspects like oxidation state of manganese,[3] crystal structure[4] and lattice strain[5] or abundance of certain structural motifs like μ-oxo-bridges,[6] or defective pseudo-cubane motifs,[7] coordinatively unsaturated metal cations,[8] or oxygen vacancies,[9] but also specific surface area,[10] or crystallinity and electric conductivity the oxide phase or are discussed as decisive factors for the activity of MnO$_x$ as water oxidation catalyst. However, it remains difficult to judge on the relative importance of these individual factors based on a comparison of literature reports as the relative activity of different samples may depend for example not only on electrode preparation and pre-conditioning[11] parameters but also on the method used to measure OER activity as was recently shown by Stahl and co-workers.[4a]

In this work, we have followed the powder approach to study different samples of the same manganese oxide phase, namely α-(K)MnO$_2$ known as cryptomelane, with two different oxidation methods, electrocatalytic OER, as well as using tetravalent cerium ammonium nitrate (CAN) as chemical oxidizing agent (CAN test). The CAN test is a well-established probe reaction[12] and was recently reviewed by Frey et al.[13] Using this approach, we can employ classical powder techniques such as powder-XRD or nitrogen physisorption for comprehensive characterization before applying the samples in water oxidation. Correlation of this characterization data with kinetic data enables identification of those materials properties that determine the catalytic activity in each type of OER catalysis, electrocatalysis and CAN test. At the same time, we can exclude phase-intrinsic factors like oxidation state, crystal phase or bulk structural motifs, and electric conductivity as being responsible for observed differences in catalytic activity as these are nominally the same for all samples. Hence, this approach allows studying the effects of microstructural properties resulting from their different preparation history.

When comparing different manganese oxides, cryptomelane has been found by some groups but not all as a promising catalyst.[14] Cryptomelane crystallizes in the hollandite or α-MnO$_2$ structure type. It consists of edge-sharing MnO$_6$ octahedra, which form 2×2 tunnels with a spacing of the wall atoms of 4.8 Å (Figure S1 in Supporting Information).[15] The average oxidation state of the manganese is slightly below +4, caused by a mixed valence.[13, 16] Usually, foreign cations are located in the tunnels making these materials an interesting cation exchanger.[17] The preferred tunnel cation of the hollandite-type MnO$_2$ phases is potassium. The related mineral of the resulting K-hollandite α-(K)MnO$_2$ is called cryptomelane,[18] a term that is used in this work for our synthetic samples. Cryptomelane is of interest as electrode in lithium batteries[19] or catalyst for the oxidative degradation of volatile organic compounds.[20] Several methods for its synthesis were developed and reported. In the following, only a few that are relevant for this work are named. The treatment of α-Mn$_2$O$_3$ (Bixbyite) with an acidic potassium ions containing solution leads to a precipitation of cryptomelane.[21] Golden et al. transformed δ-MnO$_2$ (Birnessite) to cryptomelane by thermal treatment.[22] Other well established routes are based on the use of potassium permanganate as precursor, such as refluxing,[16a] hydrothermal treatment,[23] or a solvent-free calcination of a KMnO$_4$/Mn$^{2+}$-salt mixture.[24] We have made use of these five different literature-reported low-temperature routes towards cryptomelane providing a sample series with identical ideal structure, but different texture and microstructure, which enable identification of the decisive materials properties that make cryptomelane an active OER catalyst.

## Results and Discussion

Five different variants of cryptomelane were synthesized by different methods and labelled after their synthesis R- (reflux), PHT- (precursor hydrothermal), HT- (hydrothermal), PC- (precursor calcination), and SS-cryptomelane (solid state). Full details on the syntheses are given in the experimental section.

### Catalytic performance

A comparative study of these five samples was conducted by electrochemical OER after depositing the powders on a glassy carbon electrode, and by chemical water oxidation using a suspension of the powders in the CAN test. The results of the electrocatalytic measurements in alkaline electrolyte (1 M KOH) plotted in Figure 1 cover a wide range of OER activities and show strong differences among the differently synthesized cryptomelane samples. The most active catalyst R-cryptomelane reached a current density of about 30 mA cm$^{-2}$ at 1.8 V, in contrast to SS-cryptomelane which exhibited the lowest value < 5 mA cm$^{-2}$. The potential required to reach a current density of 10 mA cm$^{-2}$, which is often used as performance indicator for OER, is 1.73 ± 0.02 V for R-cryptomelane and thus comparable to values reported in the literature.[1d] However, as 10 mA cm$^{-2}$ was not reached by all catalysts, the current density at 1.8 V is used as performance indicator in this comparative study.

Interestingly, if the five samples are tested in the CAN test with Ce$^{4+}$ as chemical oxidizing agent at pH ≈ 2, the observed trend changes. Figure 2 shows the catalytic activities as initial O$_2$ evolution rate. Again, strong differences between the five samples are observed with the lowest value of only around 1 µmol min$^{-1}$ whereas the highest rate can be found at about 10 µmol min$^{-1}$. This best value in the CAN test was achieved by the SS-cryptomelane, which showed the poorest activity in electrochemical OER. The sample which exhibited the poorest performance in the CAN test was HT-cryptomelane, which showed an intermediate activity in electrocatalysis. In both
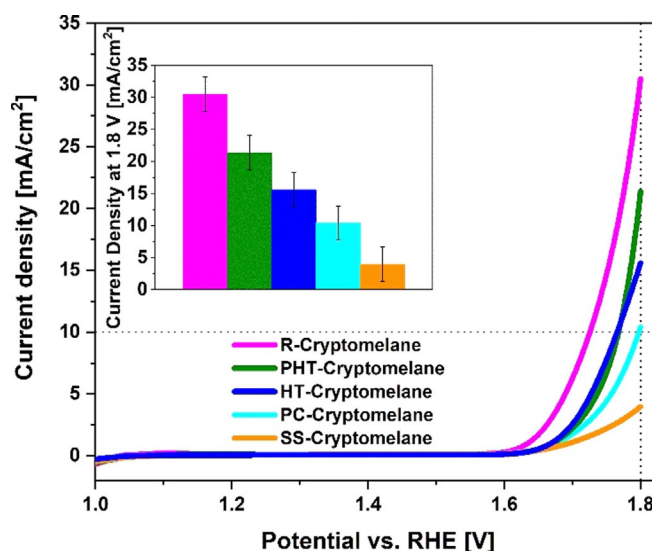


**Figure 1.** OER activities of different cryptomelane catalysts as rotating disk electrode voltammograms recorded in 1 M KOH at 5 mV s$^{-1}$ scan rate and 1600 rpm rotation speed, and as current density at a voltage of 1.8 V (inset). The error bars describe the standard deviation of five measurements for the most active catalyst.
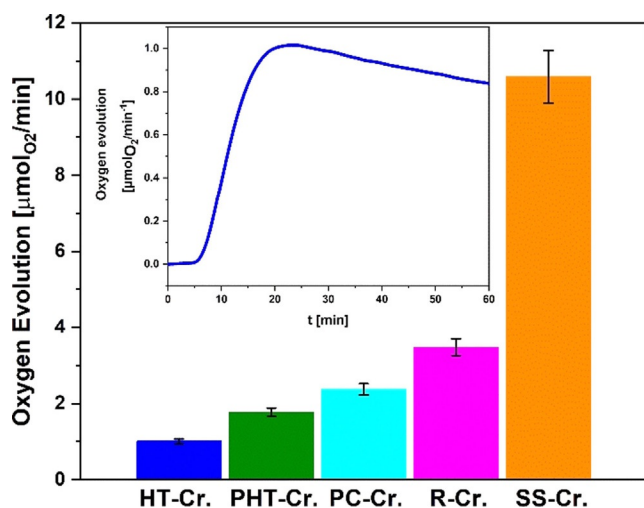
**Figure 2.** Initial rate of oxygen evolution during chemical water oxidation using $Ce^{4+}$ as chemical oxidizing agent (CAN test). The inset shows the course of an experiment over 60 min for the example of HT-cryptomelane. The initial rate was determined as the maximum of this curve. The error bars were determined as described in the experimental section.

tests the samples catalyse the oxidation of water by either an externally applied potential or by a redox potential as driving forces. To understand the different order of the sample series in the two tests, the samples were carefully characterized to explain these two different observed trends.

## Catalyst characterization

Firstly, to verify the phase identity, XRD patterns of each sample were recorded (Figure 3, Figure S2). Powder XRD indicates no other crystalline phases than the hollandite-type structure of cryptomelane. It thus can be excluded that the presence of different crystal phases or bulk structural motifs
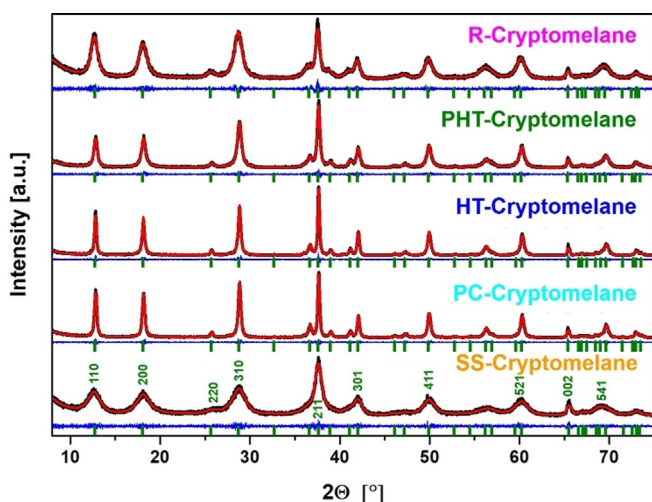


**Figure 3.** Graphical results of the Rietveld refinement of the powder diffraction data of the different cryptomelane samples (black symbols: experimental data points, red line: calculated intensities, blue line: difference between experimental and calculated data, green tick marks: positions of Bragg peaks).

serves as explanation for the differences in catalytic performance. However, differences are present in the peak profiles. The patterns of PHT-, HT- and PC-cryptomelane show very discrete and sharp reflections, and those peaks with relatively low intensity are also clearly detected. In contrast, the patterns of the R- and SS-cryptomelane exhibit broad peaks with lower intensity, but still clearly assignable to $\alpha$-$MnO_2$. The dissimilar peak widths can be interpreted as differences in the microstructure such as crystallite size or strain effects or a varying defect density in the crystal. The co-existence of broad and narrow in some patterns, for example, R-cryptomelane, serves as a first indication for anisotropic structural features in at least some samples. Rietveld refinement of the powder diffraction data leads to satisfying goodness factors (Table S1). Selected structural data and results of the refinements are summarized in Table 1.

To quantify the size effects, the global volume-weighted mean column height (LVol-IB) was calculated. This value correlates with the grain or crystallize size (although not necessarily with the particle size) and thus inversely with the number of grain boundaries and the peak width. The data in Table 1 show that the synthesis method strongly affects the grain size of the product. The LVol-IB value varies almost by an order of magnitude and ranges between 6 and 58 nm. The differences in the lattice parameters of the cryptomelane samples on the other hand are rather small. The value of the c-parameter was calculated to be approximately 2.85 Å for all samples, whereas the a/b parameter ranges between 9.80 and 9.83 Å, which may indicate variations in the widening of the 2×2 tunnels. However, the patterns with broad reflections (R-, and SS-cryptomelane) exhibit a higher uncertainty of the lattice parameters apparent from the estimated standard deviations in Table 1 and are thus difficult to interpret properly. The XRD patterns showed differences in the relative intensities of some reflections, which may be explained by a preferred orientation of anisotropic crystallites. Indeed, the goodness-of-fit of the Rietveld refinement can be further optimized by taking into account a preferred growth along the <00$l$> direction and, consequently, a preferred orientation of crystallites with a needle-like shape (R-, PHT, HT-cryptomelane). The growth direction of the needles is the c-axis along the direction of the tunnels. This anisotropic morphology is typical for cryptomelane, consistent with the

**Table 1.** Lattice parameters and crystallize sizes of the five different cryptomelane samples obtained by Rietveld refinement. All samples crystallized in the $\alpha$-$MnO_2$ structure type (tetragonal, space group: $I4/m$) with 8 formula units in the unit cell.

| Sample | $a = b$ [Å] | $c$ [Å] | LVol-IB [nm][a] |
|---|---|---|---|
| R-cryptomelane | 9.83(8) | 2.85(2) | 9(6) |
| PHT-cryptomelane | 9.819(6) | 2.8554(17) | 19(5) |
| HT-cryptomelane | 9.8062(19) | 2.8526(5) | 48(9) |
| PC-cryptomelane | 9.810(2) | 2.8536(6) | 58(15) |
| SS-cryptomelane | 9.8(2) | 2.85(6) | 6(19) |

[a] The crystallite size was calculated as volume-weighted mean column height from the integral breadths of the diffraction peaks.

**Chemistry–A European Journal**

**Full Paper**
doi.org/10.1002/chem.201905090

**Chemistry Europe**
European Chemical
Societies Publishing

observed anisotropic size broadening of *hkl* peaks with $l=0$, and also observed in this study by SEM (Figure 5, see below).

For further structural characterization, Raman spectra of R- and HT-cryptomelane were recorded representing the samples with anisotropically broadened and relatively uniformly narrow XRD peaks, respectively. The results are shown in Figure 4 and Table S2. Both samples exhibit Raman peaks at positions previously reported for $\alpha$-(K)MnO$_2$[25] and confirm the result of the XRD phase analysis with regard to the identical bulk structure of both samples. The presence of the peaks at $\approx$580 and $\approx$640 cm$^{-1}$ indicates a well-defined hollandite-type tetragonal structure, and are caused by symmetric vibrations of the manganese-oxygen bonds,[25a,c] while the low intensity bands found between 280 and 520 cm$^{-1}$ rather originate from deformation modes.[25b] The intense peak centred at $\approx$185 cm$^{-1}$ differentiates $\alpha$-MnO$_2$ from other MnO$_2$ structures and can be assigned to translational motion of the MnO$_6$ octahedra.[25b] The weak peak at 759 cm$^{-1}$ was found in the case of R-cryptomelane at very low intensity, but it was not detected in the HT-cryptomelane sample. According to the literature, it is related to the antisymmetric Mn–O stretching vibrations.[25a,c]

SEM images of the samples are shown in Figure 5. In agreement with the XRD results, the morphology of R-, PHT- and HT-cryptomelane can be clearly described as needle-like. PC- and SS-cryptomelane samples give a first impression of a sponge-like morphology, however, in a higher resolution also elongated crystals or short needles can be seen. This shape has been reported in many studies on this material with the needles being orientated along the crystallographic *c*-axis.[26] To quantify the morphologic properties, the average length and width of the particles in the SEM images were measured to gain the average aspect ratio (Table 2). Depending on the synthesis route, the particle size varied in a large range. The mean needle lengths ranged between 40 and 580 nm and the mean needle widths between 60 and 20 nm, resulting in a variation of the aspect ratio between 2 and 15. This variation is mainly caused by the needle length, rather than by changes in the needle width. In general, the needle growth seems to benefit from wet synthesis conditions during the cryptomelane crystallization step, whereas the lowest aspect ratios were found for the dry syntheses of PC- and SS-cryptomelane.
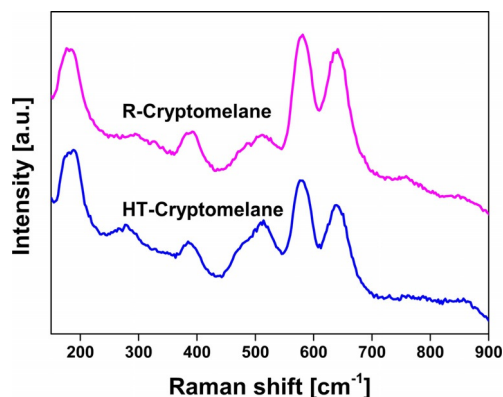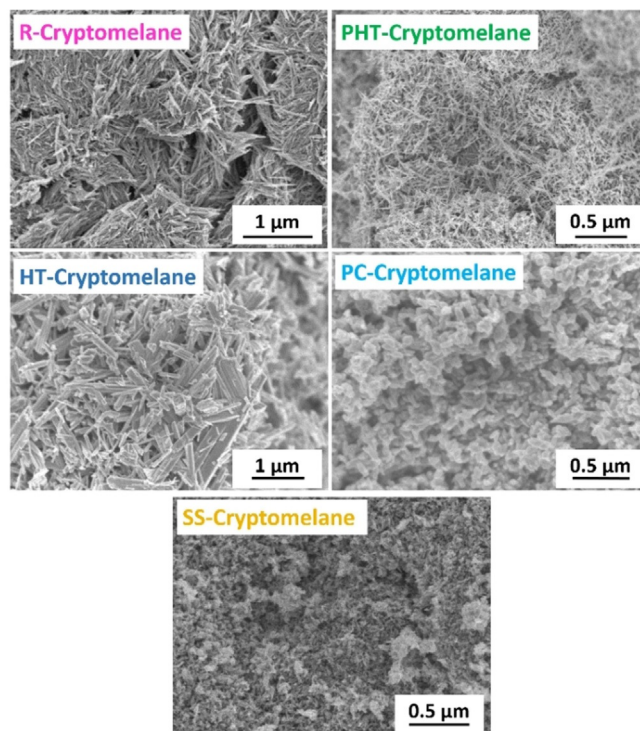


**Figure 5.** Scanning electron micrographs of the different cryptomelane samples.

**Table 2.** Specific surface area, double layer capacitance, textural properties and elemental composition of the five cryptomelane samples.

| | $S_{BET}$ [m$^2$ g$^{-1}$] | $C_{DL}$ [mF] | $L$[a] [nm] | $W$[b] [nm] | $L/W$ | Chemical formula[c] |
|---|---|---|---|---|---|---|
| R | 94 | 0.56 | 584$\pm$293 | 37$\pm$14 | 16$\pm$10 | K$_{0.10}$MnO$_{1.95}$·0.30 H$_2$O |
| PHT | 45 | 0.235 | 566$\pm$238 | 49$\pm$17 | 12$\pm$6 | K$_{0.12}$MnO$_{1.96}$·0.22 H$_2$O |
| HT | 9 | 0.135 | 418$\pm$321 | 64$\pm$34 | 7$\pm$6 | K$_{0.13}$MnO$_{1.97}$·0.01 H$_2$O |
| PC | 39 | 0.11 | 114$\pm$39 | 43$\pm$14 | 3$\pm$1 | K$_{0.13}$MnO$_{1.97}$·0.14 H$_2$O |
| SS | 166 | 0.095 | 45$\pm$15 | 20$\pm$4 | 2$\pm$1 | K$_{0.10}$MnO$_{1.95}$·0.57 H$_2$O |

[a] Average needle length and [b] width as determined by SEM. The error refers to the standard deviation due to the particle size distribution, which exceed the uncertainty of the measurements. [c] Cationic composition derived from AAS. The oxygen content was obtained from the difference to 100% of the total elemental composition. An average manganese oxidation state of +3.8 was assumed according to literature data[13] to discriminate between lattice oxygen and crystal water.

The thermogravimetric analysis revealed different amounts of moisture in the samples, but otherwise the expected stepwise decomposition into $\alpha$-Mn$_2$O$_3$, $\delta$-MnO$_2$ and Mn$_3$O$_4$ upon heating in air was observed. These results are displayed and discussed in detail in the Supporting Information (Figure S3).

The BET surface areas of the examined cryptomelane samples were found to strongly depend on the synthesis route. The results obtained by nitrogen physisorption are listed in Table 2. The surface area ranged between 9 and 170 m$^2$ g$^{-1}$ at an estimated error of $\pm$1 m$^2$ g$^{-1}$. The chemical composition regarding manganese and potassium was measured by atomic absorption spectroscopy (AAS) at high precision. The K/Mn



**Figure 4.** Raman spectra of R- and HT-cryptomelane.

**Chemistry–A European Journal**

Full Paper
doi.org/10.1002/chem.201905090

**Chemistry Europe**
European Chemical
Societies Publishing

ratio is only slightly influenced by the synthetic route and similar to previously reported data.[27] The oxygen content is obtained from the difference to 100% of the total elemental composition. The lattice bound oxygen is calculated by assuming an average manganese oxidation state of +3.8[13] (+1 for potassium). The remaining oxygen is attributed to $H_2O$ or OH-groups. The so-determined moisture content correlates with the BET surface area of the samples indicating that the differences are likely due to surface-bound species. This is further supported by thermogravimetric analysis (Figures S3, S4), where the early mass loss detected between 50 and 300 °C was found to correlate with the BET surface area and the calculated water content. This suggests that differences in $n$ of $MnO_2 \cdot n H_2O$ in Table 2 can be explained with differences in the exposed surface area and the different amount of $H_2O$ or OH adsorbed there (Figure S4), while the bulk composition of all cryptomelane samples is rather similar.

The electric conductivity was measured for selected samples using the four-point probe technique on cold-pressed powders. The low stability of the pellets prevented measuring the complete series of samples and reliable data were only obtained for R-, HT-, and SS-cryptomelane. The curves in Figure 6a, whose slopes are inversely proportional to the electric conductivity, show strong differences between the three catalysts. The measurements were conducted without heat treatment of the pellets and the absolute values are likely affected by grain boundary effects. However, a semi-quantitative comparison revealed that the measured conductivity was highest for R-cryptomelane, while it reached only one half and one third for HT- and SS-cryptomelane, respectively. The double layer capacitance ($C_{DL}$), which is proportional to the electrochemically active surface area, was also determined for all cryptomelane samples by cyclic voltammetry recorded in the non-Faradaic potential region at different scan rates in 1 M KOH solution (Figure 6b, Table S3). Large differences were observed with the highest values for R-, PHT- and HT-cryptomelane.

In summary, while the synthesis route did not influence the bulk structure of cryptomelane as evidenced by Raman spectroscopy and XRD, the particle size and shape were significantly affected. Differences were observed in the aspect ratio of the needles, the BET surface area, the conductivity of the powder pellets, and the electrochemically active surface area of the catalyst layer as represented by the double layer capacitance. The observed differences in composition regarding the oxygen content are however correlated with the exposed surface area and, thus, can be assigned to surface OH-groups and/or adsorbed water.

## Factors governing catalytic performance

The observed performance trend among the five catalysts was different for electrochemical OER and for the CAN test suggesting that different factors govern the oxygen evolution depending on the experimental driving force for water oxidation. Thus, the measured trends in the materials properties described above are now compared to the activity trends with the aim to find correlations.
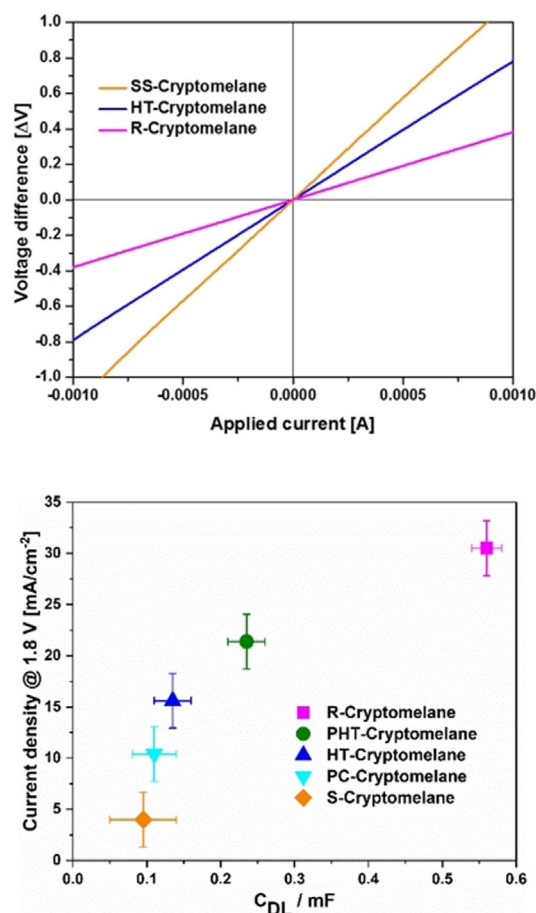


**Figure 6.** Resistivity measurement of selected cryptomelane samples (a) Double layer capacitance ($C_{DL}$) of the different cryptomelane samples determined by cyclic voltammetry recorded in the non-Faradaic potential region at scan rates of 0.01, 0.05, 0.1, 0.15 and 0.2 V s$^{-1}$ (b) The charging currents measured at 1.32 V vs. RHE during both the anodic and the cathodic scan were plotted as a function of the scan rate. The absolute value of the slopes obtained from a linear fit are reported as $C_{DL}$. All measurements were carried out in 1 M KOH solution.

In the CAN test, an obvious candidate for a strongly influencing factor is the exposed surface area as determined by nitrogen physisorption with the BET method. Indeed, a clear and almost linear correlation is observed between the initial catalytic rate and the exposed surface area (Figure 7a).

Additional catalytic tests have been performed using the decomposition of hydrogen peroxide, a reaction that is relatively facile compared to water oxidation and in which manganese oxides are known to be among the best performing solid catalysts. Indeed, considerably higher OER rates have been detected in the case where $H_2O_2$ was used as oxygen source. In this test reaction, a good correlation between the exposed surface area and the initial rate has been observed (Figure S5). These results suggest that the OER proceeds in both cases in an apparently structure-insensitive manner as one may have expected for the fast radical $H_2O_2$ decomposition. For the more complex four electron oxidation of $H_2O$, this result is remarkable. A correlation with particle morphology could not be observed as shown by the attempt to plot the initial OER rate in the CAN
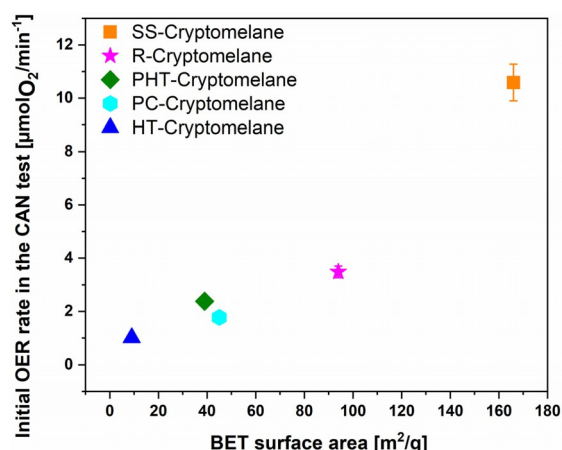
**Chemistry–A European Journal**

Full Paper
doi.org/10.1002/chem.201905090

**Chemistry Europe**
European Chemical
Societies Publishing

**Figure 7.** Initial OER rates in the CAN test plotted versus the exposed surface area determined by nitrogen physisorption. The error for the physisorption measurement is of the order of $\pm 1\ m^2\,g^{-1}$ and the error bars do not exceed the symbol sizes.

test over the aspect ratio as shown in Figure S6. Based on these observations, we can assume that the OER in the CAN reaction on cryptomelane is intrinsically slower, but similarly independent of the particle morphology as the $H_2O_2$ decomposition reaction, for which structure-insensitivity is assumed.

All differences in activities are thus best explained by a higher exposed surface area, indicating either that all geometric configurations on the different surface facets of the cryptomelane needles contribute equally to the OER (structure insensitive catalysis) or that all surface facets have been transformed under reaction conditions into sites of similar activity independent of their initial geometric configuration (structure insensitive surface dynamics). In the light of the frequent observations of dynamic changes of the (surface) structure of manganese oxides under OER conditions reported in the literature,[1e,f, 6a, 28] and expected according to the Pourbaix diagram,[29] the latter view seems more plausible.

The situation was different when the kinetic data of the electrocatalytic OER was taken to search for correlations. In this case, no correlation with the exposed BET surface area (Figure S7), but a dependence of the performance on the aspect ratio and the double layer capacitance ($C_{DL}$) was observed as shown in Figure 8. On a first sight, the almost linear correlation in Figure 8a suggests different activity of different exposed crystalline facets in terms of a structure-sensitive reaction. As the OER was improved for a higher aspect ratio, that is, for longer and thinner needles, the sides of the needles appear to be more active than their tips. Indeed, Selvakumar et al. suggested an influence of the particle morphology of $\alpha$-$MnO_2$ on the OER performance with the help of density functional theory.[30] The authors calculated an affinity of the 310 surface terminations toward water molecules and related it to an enhanced catalytic OER activity and proposed that a nano-wire or needle morphology exhibits a higher exposure of these planes to the reaction interface. This result seems to explain our observation, that the OER activity increases parallel to the aspect ratio although dynamic changes of the surface under reaction
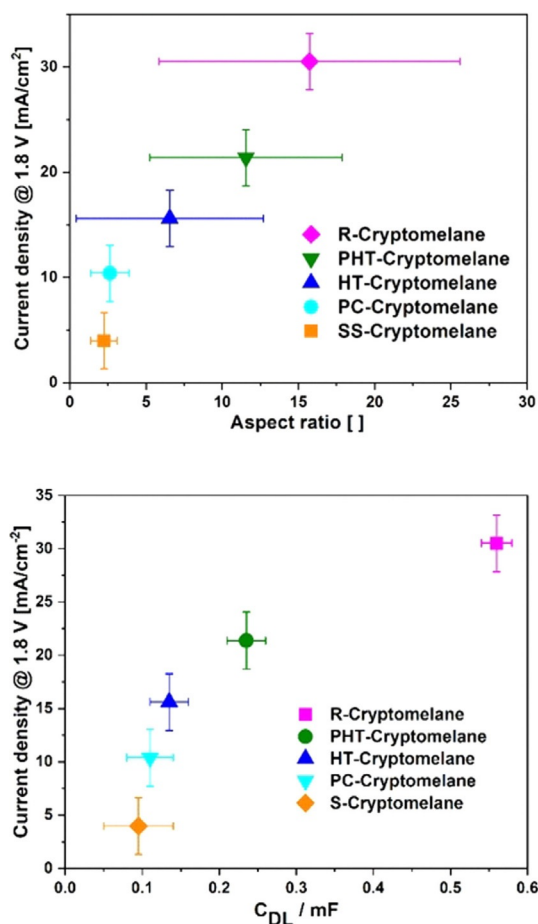




**Figure 8.** Correlation of electrocatalytic OER activity with the mean aspect ratio of the needle-like particles (a) and the double layer capacitance (b) of the different cryptomelane catalysts.

conditions, which are likely to occur, are not considered. However, based on the Wulff construction calculated by Tompsett et al.,[9b] the long sides of $\alpha$-$MnO_2$ needles are rather terminated by low-indexed 100 and 110 surfaces, while the higher indexed facet terminates part of the needle tips. Furthermore, if such difference in activity of individual facets exists, it remains unclear why this structure-sensitivity did not affect our CAN test data, which does not support the existence of such large differences between individual surface facets (Figure 7).

Including the origin of the plot shown in Figure 8b, an almost linear correlation between the OER performance and the $C_{DL}$ for the first four catalysts becomes apparent indicating the same specific activity of these catalysts. The performance of the most active catalyst R-cryptomelane seems a bit lower than expected based on the $C_{DL}$. Differences in specific OER activity have been observed for different polymorphs of $MnO_2$ and different manganese oxides/hydroxides.[4b,c, 7, 11, 28] For our differently prepared $\alpha$-$MnO_2$ catalysts, the correlation between OER activity and $C_{DL}$ (Figure 8b) speaks for a rather similar specific activity of all catalysts in agreement with the CAN test results.

With regard to the different trends observed for electrochemical and chemical OER, a prominent difference between

**Chemistry–A European Journal**

Full Paper
doi.org/10.1002/chem.201905090

**Chemistry Europe**
European Chemical
Societies Publishing

CAN test and electrocatalytic OER is the relevance of electric conductivity, which is required for the removal of electrons through the catalyst layer in electrochemistry, but much less relevant in the CAN test as the catalyst particles are immersed in an aqueous solution of $Ce^{4+}$, which can act as electron scavenger directly at the location of catalytic turnover. According to these considerations, the surface sites in electrocatalytic OER may also be similarly active as seen in the CAN test, but not equally well connected to the back contact of the electrode and a correlation between conductivity on the catalyst layer level and particle morphology should exist. Indeed, plotting the relative electric conductivity versus the aspect ratio of the particles results in a linear correlation as shown in Figure 9a. This correlation can explain the differences in OER activity considering an effect of particle morphology on conductivity rather than on the intrinsic kinetics as demonstrated in Figure 9b.

This scenario is in line with the results of the CAN test (Figure 7) and the similar specific OER activity (Figure 8b) suggesting a similar activity of different surface facets, but it emp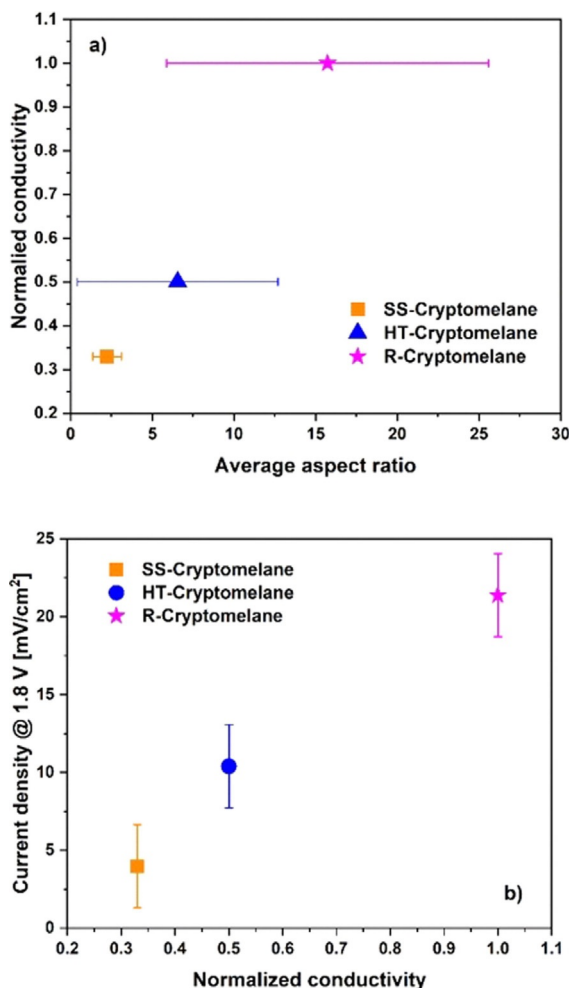hasizes the large kinetic limitation by the electron transport through the drop-casted catalyst layer that completely disguises a correlation between electrocatalysis and the exposed BET surface area (Figure S7). In order to evaluate our sample series for this limitation, the powder sample have been mixed with the same amount of carbon black (VULCAN XC72R, Quintech) in a weight ratio of 2:1 to improve conductivity without affecting the particle morphology. The electrocatalytic measurements were repeated with these composites and revealed a substantial improvement of the OER activity due to the soot addition (Figure 10). Such an effect is well-known and has been employed, for example, for the preparation of highly active manganese oxide/carbon heterostructures.[31] Importantly, the overall trend was not changed, but the activities of the different cryptomelanes tend to converge as can be seen from the higher performance increase for the lower active catalysts. The highest increase was 555% for the SS-cryptomelane with initially low conductivity but high specific surface area, while the initially most-active catalyst did not even double its activity (174%). The best and the worst catalysts differ by a factor of 7.7 before (30.50 and 3.98 mA cm$^{-2}$ at 1.8 V), but only a factor of 2.4 after addition of carbon black (53.08 and 22.11 mA cm$^{-2}$ at 1.8 V). The OER improvement by addition of carbon black was thus higher for catalysts exhibiting an initially low conductivity compared to those whose conductivity was already relatively high. This result confirms the general limiting role of electric conductivity in electrocatalytic OER on drop-cast powder layers and provides support for a similar surface activity of all cryptomelane catalysts that may lead to a similar (or rather surface area-dependent) electrocatalytic OER per-
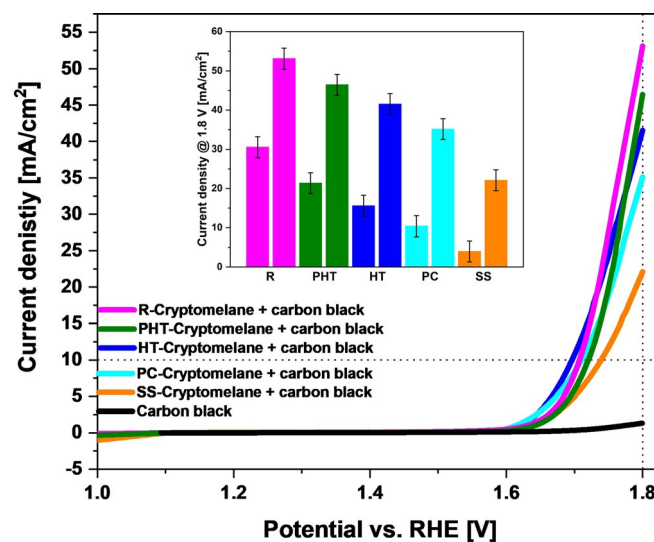


**Figure 9.** Correlations between the normalized conductivity of selected cryptomelane catalysts and the aspect ratio of the needle-shaped particles (a). Correlation of the electrocatalytic OER activity with the normalized conductivity (b). The lines are only guides to the eye.



**Figure 10.** OER activities of the cryptomelane catalysts after mixing with carbon black as rotating ring disk electrode voltammograms and comparison of the current density at a voltage of 1.8 V before and after carbon black addition (inset). Improvement of the electrocatalytic OER by addition of carbon black expressed as current density observed at 1.8 V with carbon black containing samples divided by the same value obtained with the samples without carbon black as a function of the normalized conductivity of selected catalysts.

formance only if all catalyst electrodes were made equally conductive.

This view still requires an explanation for the observed correlation between conductivity and particle morphology (Figure 9a). Two possible scenarios seem likely. First, the electric conductivity may be highly anisotropic and facilitated along the directions of the tunnels of the $\alpha$-MnO$_2$ structure, that is, the growth direction of the needles, as suggested for example by Byles et al.[32] In this case, particles with high anisotropy in the drop-casted powder layer may favour paths for the electrons to travel easier through an aggregate compared to isotropic particles. Secondly, the effect might be due to the lower electric resistivity within a crystalline particle opposed to the grain boundaries connecting neighbouring particles. In this case, longer needles enable a better electron transport as compared to shorter needles that require more grain boundaries for a given distance in the powder layer.

To decide for one of these models, we have employed theory to explore the anisotropy of conductivity in the cryptomelane structure. The calculations result in values of $5.4 \times 10^4$ S m$^{-1}$ in the crystallographic $a/b$-directions and a lower value of $2.5 \times 10^4$ S m$^{-1}$ in the $c$-direction of single crystals. For powders markedly lower values can be expected and, indeed, the experimental data in the literature ranges from 0.1 to 1 S m$^{-1}$ for four point probe measurements of thin films[33] to 225.9 S m$^{-1}$ for a single $\alpha$-MnO$_2$ nanowire measured along the crystallographic $c$-axis.[32] However, the calculations do not support an anisotropy of conductivity on the particle level favouring the long dimension the needles ($c$-direction). They rather support the second model and suggest a correlation of the conductivity with the absolute needle length highlighting the importance of extrinsic ensemble effects at grain boundaries in the OER measurement on drop-casted electrodes. This effect can also be assumed to be responsible for the large difference in the measured conductivities of thin films and single needles found in the literature.

An additional parameter that was reported to improve the electrocatalytic performance of manganese oxides in OER and ORR is thermal annealing.[14, 34] We tested this parameter for the example of the PHT-cryptomelane catalyst, which was calcined at 400 °C after hydrothermal treatment. As shown in the Supporting Information (Figures S8, S9), this did not significantly change the particle morphology. However, the OER performance was substantially improved as recently also reported by Antoni et al.[14] In our model, this may be due to improved electric conductivity of the needles as a result of defect annealing during the thermal treatment. However, several studies reported rather an increase in the charge transfer resistance $R_{ct}$ determined by impedance spectroscopy,[14, 35] and further work is needed to unambiguously clarify the possible effects of thermal annealing.

In summary, our comparative study revealed that the OER activity observed in the CAN test is almost exclusively governed by the exposed surface area of the cryptomelane catalysts as measured by nitrogen physisorption (Figure 7), while the OER activity in electrocatalysis was almost exclusively governed by the electrical conductivity (Figure 9b). In the powder

layers, the latter is strongly dependent on particle morphology, which can be controlled by the synthesis method of the respective cryptomelane catalyst and can be further improved by addition of a conductive additive such as carbon black.

## Catalyst stability

Catalyst stability is a very critical issue for the application of new materials in water electrolysis. The deactivation of R- and HT-cryptomelane as highly and moderately active catalysts was investigated by applying a potential of 1.8 V for 60 min while the current density was monitored. For comparison, degradation is expressed as normalized current density loss in Figure 11. The reproducibility of the stability data is confirmed by repeated measurements shown Figure S11 in the Supporting Information including the stability measurements of the other cryptomelane catalysts PHT, PC and SS (Figure S12).

Both catalysts showed the same response with the strongest activity loss occurring during the first minutes. After a reaction time of approximately 5 min the detected current flow already drops to half of the starting value and falls to zero after 45 min showing a poor stability of the cryptomelane powders that is prohibitive of any application. To understand the reason for the fast breakdown of activity, the structural stability during catalysis was investigated by operando electrochemical Raman spectroscopy and ex-situ powder XRD of the spent catalyst. Figure 12a shows the Raman spectra of HT-cryptomelane recorded at different potentials. The main bands of the spectra are observed at the same position and with similar relative intensities as already seen in Figure 4 and do not change much with increasing potential. This suggests that the bulk is stable under reaction conditions. This was confirmed based on the XRD of the catalyst after an operation time of 10 min at 1.8 V, which corresponds to a deactivation of approximately 65%. The Rietveld refinement of the powder scratched off the electrode is shown in Figure 12b and the results are compiled in Table 3. The low reflection intensities and the high background
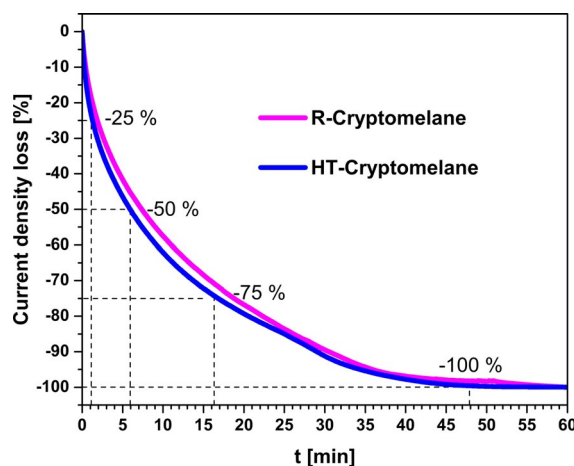


**Figure 11.** Stability test showing the loss of OER activity over time. The current density was monitored while applying a constant potential of 1.8 V vs. RHE, using 1 M KOH as electrolyte and an electrode rotation of 1600 rpm.
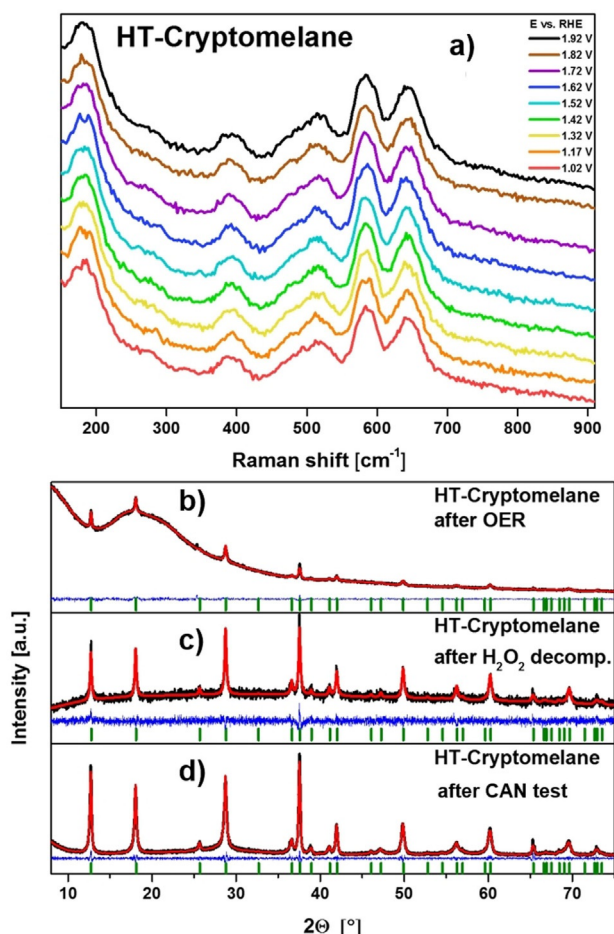
**Chemistry–A European Journal**

**Full Paper**
doi.org/10.1002/chem.201905090

**Chemistry Europe**
European Chemical
Societies Publishing

**Figure 12.** Raman spectra of HT-cryptomelane recorded in situ at different potentials in the range from 1.02 to 1.92 V vs. RHE, measured in 0.01 M KOH (a) and graphical results of the Rietveld refinement of the powder diffraction data of HT-cryptomelane after OER measurement (b), after $H_2O_2$ decomposition (c) and after water oxidation catalysis (d).

**Table 3.** Lattice parameters of the five HT-cryptomelane before catalysis, after 10 min electrocatalytic OER, after $H_2O_2$ decomposition and after the CAN test as obtained by Rietveld refinement.

| Sample | $a=b$ [Å] | $c$ [Å] |
|---|---|---|
| before catalysis | 9.8062(19) | 2.8526(5) |
| after electrocatalysis | 9.835(11) | 2.857(3) |
| after $H_2O_2$ decomposition | 9.799(3) | 2.8528(8) |
| after CAN test | 9.807(3) | 2.8522(7) |

these might be tentatively related with the widening of the tunnels, which are only observed under applied external potential in the alkaline electrolyte. However, surface effects likely play an important role in the deactivation of cryptomelane during OER, and dynamic changes[1f, 6a, 28] as well as corrosion[1e] have been observed in several studies. Anyway, further investigations are needed to draw reliable conclusions on the reasons for catalyst degradation.

## Conclusions

Cryptomelane ($\alpha$-(K)MnO$_2$) was successfully synthesized by different methods. Raman spectroscopy and XRD patterns indicated phase-pure samples crystallizing in hollandite-type structure and only slight variations of the lattice parameters could be observed. Also the potassium content varied only in a small range from 10 to 13 cation-%. In contrast, the BET surface area (9 to 166 m$^2$g$^{-1}$) and the crystallize size (6 to 58 nm) covered a broader range indicating strong differences in the microstructure of the different catalysts. Their morphology was needle-like, and the exact shape and the particle size strongly depended on the synthesis route. The aspect ratio of the needles varied between 2 and 16. Comparative measurements pointed out a substantial influence of the synthesis method on the catalytic performance in the OER despite the presence of the same crystallographic phase. Water oxidation catalysis with Ce$^{4+}$ as chemical oxidizing agent (CAN test) and electrocatalytic OER experiments showed a different activity sequence of the tested catalysts. The decisive microstructural factors that explain this difference were identified: The CAN test activity is substantially governed by the exposed surface area, while the electrocatalytic activity is determined largely by the electric conductivity. Interestingly, the latter was found to correlate with the needle length and the aspect ratio in our sample series. This correlation is rather explained by an improved conductivity due to longer needles than by structure sensitivity as was supported by reference experiments using $H_2O_2$ decomposition and carbon black as additive. The most active catalyst R-cryptomelane reached a current density of 10 mA cm$^{-2}$ at 1.73 V without, and at 1.71 V with the aid of carbon black. However, the catalysts showed a disappointing catalytic stability during alkaline electrochemical OER, while the crystal structure was found to be stable under working conditions.

## Experimental Section

**Synthesis and sample labelling**: The **R-cryptomelane** (R for reflux) synthesis was adapted from DeGuzman et al.[16a] 2.76 g Mn(Ac)$_2$·4H$_2$O (>99% p.a., Fluka Chemie AG), 200 mL KMnO$_4$ (>99% p.a., Carl Roth GmbH) solution (0.037 mol I$^{-1}$) and 3 mL HNO$_3$ (65%, Fisher Chemicals) were stirred (500 rpm) in a 250 mL round-bottom flask connected to a water-cooled condenser open to the atmosphere at the top. The solution was heated to 100 °C (reflux) for 24 h.

The **PHT-cryptomelane** (PHT for precursor hydrothermal) sample was obtained by a two-step synthesis. First, an amorphous precursor was precipitated by combining 300 mL of a 0.15 M

in Figure 12b are caused by the small amount of catalyst used in electrocatalysis and subsequently for the XRD measurement. The only structural change detected was an increase of the $a/b$-parameter indicative of a widening of the tunnels. The loss of activity during the CAN test was significantly lower over approximately 40 min of observation (ca. 20%, inset in Figure 2) and no noteworthy changes in crystal structure were observed (Figure 12d, Table 3) and the same is true for HT-cryptomelane spent in the $H_2O_2$ decomposition (Figure 12c, Table 3). Thus, if bulk effects are discussed as reasons for the instability in OER,

$Mn(Ac)_2 \cdot 4H_2O$ solution and 300 mL of a $KMnO_4$ solution (0.1 mol l$^{-1}$) in a beaker while stirring (500 rpm) at room temperature for 15 h. The precipitate was washed with demineralized water until the conductivity of the filtrates fell below 20 μS cm$^{-1}$ and dried in static air at 80 °C for 24 h. In a second step, the amorphous precursor was suspended in 160 mL $H_2O$ and hydrothermally treated for 48 h at 150 °C in a Teflon-lined autoclave (250 mL).

To synthesize **HT-cryptomelane** (HT for hydrothermal) analogously to the literature procedure,[36] 2 mL HCl (37%, VWR Chemicals) were added to 160 mL of a 0.1 M $KMnO_4$ solution. After stirring (500 rpm) for 30 min at room temperature the solution was hydrothermally treated for 8 h at 150 °C in a Teflon-lined autoclave (250 mL).

For the synthesis of **PC-cryptomelane** (PC for precursor calcination) the same amorphous precursor and the same first step of the synthesis route used for the preparation of PHT-cryptomelane were employed. However, the second step differed. After precipitating, washing and drying, the amorphous precursor was calcined in a muffle furnace for 24 h at 400 °C ($\beta = 20$ K min$^{-1}$) in air.

For the synthesis of **SS-cryptomelane** (SS for solid state) a solvent-free solid-state method developed by Ding et al. was used.[24] $KMnO_4$ and $Mn(Ac)_2 \cdot 4H_2O$ powders were mixed in a stoichiometric ratio of 2:3, ground in a mortar and calcined in a muffle furnace for 4 h at 80 °C ($\beta = 8$ K min$^{-1}$) in air.

All obtained powders were isolated and washed with demineralized water until the conductivity of the filtrates fell below 20 μS cm$^{-1}$. Finally, the samples were dried in static air at 80 °C for 24 h.

**Characterization**: Powder XRD patterns in the $2\theta$ range from 5 to 90° were recorded with a Bruker D8 Advance diffractometer in Bragg–Brentano geometry by using a position-sensitive LYNXEYE detector (Ni-filtered Cu$_{K\alpha}$ radiation). A step size of 0.01° and a counting time of 0.3 s were applied. Samples were dispersed with ethanol on a glass disk inserted in a round PMMA holder. The latter was subjected to gentle rotation during scanning. To verify the structure and calculate the lattice parameters a Rietveld refinement[37] was performed using the TOPAS software (Bruker).

To examine the catalysts after the electrochemical measurement by XRD the samples were recovered from the glassy carbon electrode with a commercial adhesive tape (Scotch Magic™ Tape, 3 M). After applying the catalyst on the adhesive side, the prepared tape was fixed on a glass disk in a round PMMA holder and measured by using the above mentioned setup with a step size of 0.01° and a counting time of 2.96 s.

SEM images were taken with a JEOL JSM7500F equipped with a cold-field emission gun. An acceleration voltage of 5.0 kV and an emission current of 10 μA were applied. All experiments were performed under high vacuum. Samples were fixed on a metallic holder by using a conductive carbon paste. For determining the BET surface $N_2$ physisorption experiments were performed at −196 °C with a NOVA 3200e (Quantachrome GmbH & Co. KG) after degassing the samples at 80 °C for 2 h in vacuum. BET surface areas were calculated from $p/p_0$ data between 0.05 and 0.3.

Thermogravimetric analysis (TG) and differential thermal analysis (DTA) were carried out with a Netzsch STA 449 F3 Jupiter thermoanalyzer. Powdered sample ($\approx 50$ mg) was placed in a corundum crucible and heated from room temperature to 1000 °C. A heating rate of 5 °C min$^{-1}$ and a mixture of 21% $O_2$ in Argon at a flowrate of 100 mL min$^{-1}$ were applied.

Raman spectra were recorded with a Jubin-Yvon iHR550 (HORIBA) spectrometer equipped with a 532 nm laser source (Ventus 532, Laser Quantum), using a laser power of 1 mW and a 60x objective.

Operando Raman spectroscopy experiments were conducted in a three-electrode cell configuration using a 0.01 M KOH solution as supporting electrolyte. 5 μL of catalyst powder dispersed in a mixture of water and ethanol (1:1) at a concentration of 20 mg mL$^{-1}$ were drop-cast onto a gold wafer and used as the working electrode. A platinum mesh and an Ag/AgCl (3 M KCl) were used as the counter and the reference electrode, respectively. Cyclic voltammograms were recorded until obtaining a constant response in the range from 0.1 to 0.5 V versus Ag/AgCl (1.02 to 1.42 V vs. RHE) at a scan rate of 0.1 V s$^{-1}$. Subsequently, Raman spectra were collected while simultaneously applying potentials in the range from 0.1 to 1.0 V versus Ag/AgCl (1.02 to 1.92 V vs. RHE).

The metal content of the as-prepared samples was determined by atomic absorption spectroscopy (Thermo Electron Corporation, M-Series) after dissolving the powders in hydrochloric acid.

The resistance was measured by a four-terminal sensing using a Keithley 4200 SCS parameter analyzer combined with a point probe station. The powdered samples were pressed to solid pellets with a hydraulic press (PerkinElmer, Waltham) by applying a pressure of 5 bar for 2 min. The prepared samples were contacted with four probes arranged in a line. Current was supplied by the outer probes while a voltage in the inner voltage probes were recorded. The pellets were not subjected to sintering in order to not change the sample from the state of the catalytic measurements. The low stability of the pellets prevented measurement of the complete series of samples and reliable data were only obtained for R-, HT, and SS-cryptomelane. Replicate measurements were not possible. The error due to the sample properties is estimated to exceed the measurement error of the analytic setup but could not be quantified. Using the sample method for measuring different manganese oxide references resulted in the following conductivity trend: $Mn_3O_4 > Mn_2O_3 < \delta\text{-}MnO_2 <$ all $\alpha\text{-}MnO_2$ of this study.

**Electrochemistry and Catalysis**: The electrochemical measurements were carried out in a three-electrode cell setup and a 1 M KOH solution as the electrolyte. An Autolab potentiostat/galvanostat (PGSTAT12, Eco Chemie, Utrecht, The Netherlands) coupled to a Metrohm RDE rotator (1600 rpm) was used for controlling the potentials during the measurements. A glassy carbon tip with geometric area of 0.126 cm$^2$ was used as working electrode. Ag/AgCl/ 3 M KCl and platinum foil acted as reference electrode and counter electrode, respectively. Catalyst inks were prepared by dispersing 2.5 mg of the catalyst in a solution consisting of 2 μl Nafion, 249 μl ethanol and 249 μl water, followed by 15 min ultrasonication. 5.0 μl of the ink were drop cast onto the polished glassy carbon electrode and dried in air at room temperature for about 2 h. The loaded electrodes were subjected to continuous potential cycling ($v = 100$ mV s$^{-1}$) until reproducible voltammograms were obtained before catalytic measurements ($v = 5$ mV s$^{-1}$). All reported current densities were determined based on several repeated measurements and calculated with respect to the geometric surface area of the electrode. Error bars for the electrochemical OER performance were estimated based on the standard deviation of 5 repeated measurement of the catalyst R-cryptomelane. The measured potentials were converted to the reversible hydrogen electrode (RHE) scale.[38] Double-layer capacitance ($C_{DL}$) as determined by cyclic voltammetry recorded in the non-Faradaic potential region from 1.27 to 1.37 V versus RHE at scan rates of 0.01, 0.05, 0.1, 0.15 and 0.2 V s$^{-1}$.[38a] The charging currents measured at 1.32 V versus RHE during the second anodic and the second cathodic scan were plotted as a function of the scan rate. The slopes resulting from the linear fit were extracted and their absolute values were reported as $C_{DL}$.

**Chemistry–A European Journal**

Full Paper
doi.org/10.1002/chem.201905090

**Chemistry Europe**
European Chemical
Societies Publishing

Chemical water oxidation catalysis was executed with $Ce^{4+}$ as chemical oxidizing agent. The single-electron oxidant $Ce^{4+}$ ($E^0(Ce^{3+}/Ce^{4+}) = +1.72$ V vs. NHE at pH 0) is reduced to $Ce^{3+}$ during the reaction while water is oxidized to oxygen [Eq. (1)].

$$4\ Ce^{4+} + 2\ H_2O \xrightarrow{\text{catalyst}} 4\ H^+ +\ O_2 +\ 4\ Ce^{3+} \qquad (1)$$
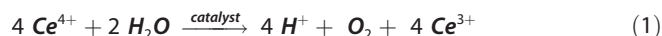
In a typical experiment 100 mg catalyst was dispersed in 45 mL $H_2O$. The reaction was conducted at pH $\approx$ 2. While bubbling Argon (50 mL min$^{-1}$) through the dispersion, 5 mL of a $(NH_4)_2Ce(NO_3)_6$ solution (2.5 mol l$^{-1}$) was added. The evolving oxygen was detected by the electrochemical oxygen analyzer EC900 (Systech Illinois). The error of our measurements was estimated based on the standard deviation of duplicate or triplicate measurements in this setup using a range of transition metal oxide benchmark catalysts coving the activity range of interest in this study resulting in a relative error of 6.5%.

**Calculations**: For the quantum-chemical model calculations, the crystal structure of cryptomelane Q ($K_{0.167}MnO_2$, ICSD 59159) was assumed.[39] The calculations of conductivity were performed based on a $1 \times 1 \times 3$ super cell model under removal of partially occupied potassium sites to reach a model composition of $K_4Mn_{24}O_{48}$ with full occupancy of the remaining K positions. The spins of manganese were assumed to couple in an antiferromagnetic manner. The electronic structure was calculated with the hybrid functional PW1PW[40] which is known to reproduce experimental electronic band gaps well.[41] The method was employed as implemented in the crystalline-orbital program CRYSTAL17 (version 1.0.2).[42] The wavefunction was expanded as linear combination of atomic orbitals. The atomic basis sets are of triple-zeta valence plus polarization quality.[43] Integration over reciprocal space was performed with a $4 \times 4 \times 4$ Monkhorst–Pack grid. For the calculation of the Fermi energy a much denser $12 \times 12 \times 12$ Gilat net was applied. The truncation thresholds for two-electron integral evaluation were increased from (6 6 6 6 12) to (7 7 7 14 42) due to our experience with hybrid functionals. The electric conductivity tensor was calculated at 293 K at the Fermi energy obtained in the SCF calculation, $-2.88$ eV, using the BOLTZTRA utility. The values reported above are the xx, yy, and zz diagonal elements of the sigma tensor. Frequency integration was performed in the interval from $-3.88$ to 1.88 eV in steps of 0.0001 eV. Much denser Monkhorst–Pack and Gilat grids ($24 \times 24 \times 24$ and $48 \times 48 \times 48$, respectively) were used (see Supporting Information for input files and basis set).

## Acknowledgements

## Conflict of interest

The authors declare no conflict of interest.

[1] a) P. Kurz, *Top. Curr. Chem.* **2015**, *371*, 49–72; b) J. Masa, W. Xia, I. Sinev, A. Zhao, Z. Sun, S. Grützke, P. Weide, M. Muhler, W. Schuhmann, *Angew. Chem. Int. Ed.* **2014**, *53*, 850–8512; *Angew. Chem.* **2014**, *126*, 8648–8652; c) A. Indra, P. W. Menezes, M. Driess, *ChemSusChem* **2015**, *8*, 776–785; d) Y. Meng, W. Song, H. Huang, Z. Ren, S.-Y. Chen, S. L. Suib, *J. Am. Chem. Soc.* **2014**, *136*, 11452–11464; e) M. Rabe, C. Toparli, Y.-H. Chen, O. Kasian, K. J. J. Mayrhofer, A. Erbe, *Phys. Chem. Chem. Phys.* **2019**, *21*, 10457–10469; f) M. F. Tesch, S. A. Bonke, T. E. Jones, M. N. Shaker, J. Xiao, K. Skorupska, R. Mom, J. Melder, P. Kurz, A. Knop-Gericke, R. Schlögl, R. K. Hocking, A. N. Simonov, *Angew. Chem. Int. Ed.* **2019**, *58*, 3426—3432; *Angew. Chem. Int. Ed.* **2019**, *131*, 3464–3470; g) C. Walter, P. W. Menezes, S. Loos, H. Dau, M. Driess, *ChemSusChem* **2018**, *11*, 2554–2561; h) M. Kölbach, S. Fiechter, R. van de Krol, P. Bogdanoff, *Catal. Today* **2017**, *290*, 2–9; i) M. Fekete, R. K. Hocking, S. L. Y. Chang, C. Italiano, A. F. Patti, F. Arena, L. Spiccia, *Energy Environ. Sci.* **2013**, *6*, 2222–2232; j) A. Indra, P. W. Menezes, I. Zaharieva, E. Baktash, J. Pfrommer, M. Schwarze, H. Dau, M. Driess, *Angew. Chem. Int. Ed.* **2013**, *52*, 13206–13210; *Angew. Chem.* **2013**, *125*, 13447–13451.

[2] a) M. S. Burke, S. Zou, L. J. Enman, J. E. Kellon, C. A. Gabor, E. Pledger, S. W. Boettcher, *J. Phys. Chem. Lett.* **2015**, *6*, 3737–3742; b) R. Subbaraman, D. Tripkovic, K. C. Chang, D. Strmcnik, A. P. Paulikas, P. Hirunsit, M. Chan, J. Greeley, V. Stamenkovic, N. M. Markovic, *Nat. Mater.* **2012**, *11*, 550–557.

[3] T. Takashima, K. Hashimoto, R. Nakamura, *J. Am. Chem. Soc.* **2012**, *134*, 1519–1527.

[4] a) R. Pokhrel, M. K. Goetz, S. E. Shaner, X. Wu, S. S. Stahl, *J. Am. Chem. Soc.* **2015**, *137*, 8384–8387; b) P. F. Smith, B. J. Deibert, S. Kaushik, G. Gardner, S. Hwang, H. Wang, J. F. Al-Sharab, E. Garfunkel, L. Fabris, J. Li, G. C. Dismukes, *ACS Catal.* **2016**, *6*, 2089–2099; c) P. K. Gupta, A. Bhandari, S. Saha, J. Bhattacharya, R. G. S. Pala, *J. Phys. Chem. C* **2019**, *123*, 22345–22357; d) D. M. Robinson, Y. B. Go, M. Mui, G. Gardner, Z. Zhang, D. Mastrogiovanni, E. Garfunkel, J. Li, M. Greenblatt, G. C. Dismukes, *J. Am. Chem. Soc.* **2013**, *135*, 3494–3501.

[5] Z. Morgan Chan, D. A. Kitchaev, J. Nelson Weker, C. Schnedermann, K. Lim, G. Ceder, W. Tumas, M. F. Toney, D. G. Nocera, *Proc. Natl. Acad. Sci. USA* **2018**, *115*, E5261–E5268.

[6] a) A. Bergmann, I. Zaharieva, H. Dau, P. Strasser, *Energy Environ. Sci.* **2013**, *6*, 2745–2755; b) I. Zaharieva, P. Chernev, M. Risch, K. Klingan, M. Kohlhoff, A. Fischer, H. Dau, *Energy Environ. Sci.* **2012**, *5*, 7081–7089.

[7] Y.-F. Li, Z.-P. Liu, *J. Am. Chem. Soc.* **2018**, *140*, 1783–1792.

[8] H. B. Tao, L. Fang, J. Chen, H. B. Yang, J. Gao, J. Miao, S. Chen, B. Liu, *J. Am. Chem. Soc.* **2016**, *138*, 9978–9985.

[9] a) K. Ganesan, P. Murugan, *Phys. Chem. Chem. Phys.* **2016**, *18*, 22196–22202; b) D. A. Tompsett, S. C. Parker, M. S. Islam, *J. Mater. Chem. A* **2014**, *2*, 15509–15509.

[10] V. B. R. Boppana, F. Jiao, *Chem. Commun.* **2011**, *47*, 8973–8975.

[11] M. Huynh, C. Shi, S. J. L. Billinge, D. G. Nocera, *J. Am. Chem. Soc.* **2015**, *137*, 14887–14904.

[12] a) C. E. Frey, M. Wiechen, P. Kurz, *Dalton Trans.* **2014**, *43*, 4370–4379; b) F. Liu, J. J. Concepcion, J. W. Jurss, T. Cardolaccia, J. L. Templeton, T. J. Meyer, *Inorg. Chem.* **2008**, *47*, 1727–1752.

[13] C. E. Frey, P. Kurz, *Chem. Eur. J.* **2015**, *21*, 14958–14968.

[14] H. Antoni, D. M. Morales, J. Bitzer, Q. Fu, Y. T. Chen, J. Masa, W. Kleist, W. Schuhmann, M. Muhler, *J. Catalysis* **2019**, *374*, 335–344.

[15] N. Kijima, T. Ikeda, K. Oikawa, F. Izumi, Y. Yoshimura, *J. Solid State Chem.* **2004**, *177*, 1258–1267.

[16] a) R. N. DeGuzman, Y.-F. Shen, E. J. Neth, S. L. Suib, C.-L. O'Young, S. Levine, J. M. Newsam, *Chem. Mater.* **1994**, *6*, 815–821; b) J. E. Post, C. W. Burnham, *Am. Mineral.* **1986**, *71*, 1178–1185; c) Q. Feng, H. Kanoh, Y. Miyai, K. Ooi, *Chem. Mater.* **1995**, *7*, 148–153.

[17] M. Tsuji, M. Abe, *Bull. Chem. Soc. Jpn.* **1985**, *58*, 1109–1114.

[18] J. W. Gruner, *Am. Mineral.* **1943**, 497–506.

[19] M. H. Rossouw, D. C. Liles, M. M. Thackeray, W. I. F. David, S. Hull, *Mater. Res. Bull.* **1992**, *27*, 221–230.

[20] a) T. Chen, H. Dou, X. Li, X. Tang, J. Li, J. Hao, *Microporous Mesoporous Mater.* **2009**, *122*, 270–274; b) X. Chen, Y. F. Shen, S. L. Suib, C. L. O'Young, *J. Catalysis* **2001**, *197*, 292–302; c) Y. Li, Z. Fan, J. Shi, Z. Liu, J. Zhou, W. Shangguan, *Catal. Today* **2015**, *256*, 178–185; d) M. T. Nguyen Dinh, J. M. Giraudon, A. M. Vandenbroucke, R. Morent, N. De Geyter, J. F. Lamonier, *J. Hazardous Mater.* **2016**, *314*, 88–94; e) L. Sun, Q. Cao, B. Hu, J. Li, J. Hao, G. Jing, X. Tang, *Appl. Catal. A: General* **2011**, *393*, 323–330.

[21] a) T. Ohzuku, M. Kitagawa, K. Sawai, T. Hiroi, *J. Electrochem. Soc.* **1991**, *138*, 360–365; b) R. Zhang, T. S. Arthur, C. Ling, F. Mizuno, *J. Power Sources* **2015**, *282*, 630–638.

[22] D. C. Golden, C. C. Chen, J. B. Dixon, *Clays and Clay Minerals* **1987**, *35*, 271–280.

[23] X. Wang, Y. Li, *Chem. Commun.* **2002**, 764–765.

[24] Y. S. Ding, X. F. Shen, S. Sithambaram, S. Gomez, R. Kumar, V. M. B. Crisostomo, S. L. Suib, M. Aindow, *Chem.Mater.* **2005**, *17*, 5382–5389.

[25] a) T. Gao, H. Fjellvåg, P. Norby, *Anal. Chim. Acta* **2009**, *648*, 235–239; b) Y. Xie, Y. Yu, X. Gong, Y. Guo, Y. Guo, Y. Wang, G. Lu, *CrystEngComm* **2015**, *17*, 3005–3014; c) T. Gao, M. Glerup, F. Krumeich, R. Nesper, H. Fjellvåg, P. Norby, *J. Phys. Chem. C* **2008**, *112*, 13134–13140.

[26] Y. Shao-Horn, S. A. Hackney, C. S. Johnson, M. M. Thackeray, *1. Electrochem. Soc.* **1998**, *145*, 582–589.

[27] T. Gao, P. Norby, *Eur. J. Inorg. Chem.* **2013**, 4948–4957.

[28] Y. Gorlin, B. Lassalle-Kaiser, J. D. Benck, S. Gul, S. M. Webb, V. K. Yachandra, J. Yano, T. F. Jaramillo, *J. Am. Chem. Soc.* **2013**, *135*, 8525–8534.

[29] H. Y. Su, Y. Gorlin, I. C. Man, F. Calle-Vallejo, J. K. Norskov, T. F. Jaramillo, J. Rossmeisl, *Phys. Chem. Chem. Phys.* **2012**, *14*, 14010–14022.

[30] K. Selvakumar, S. M. Senthil Kumar, R. Thangamuthu, G. Kruthika, P. Murugan, *Int. J. Hydrogen Energy* **2014**, *39*, 21024–21036.

[31] a) J. Melder, W. L. Kwong, D. Shevela, J. Messinger, P. Kurz, *ChemSusChem* **2017**, *10*, 4491–4502; b) H. Antoni, W. Xia, J. Masa, W. Schuhmann, M. Muhler, *Phys. Chem. Chem. Phys.* **2017**, *19*, 18434–18442; c) H. Antoni, D. M. Morales, Q. Fu, Y. T. Chen, J. Masa, W. Schuhmann, M. Muhler, *ACS Omega* **2018**, *3*, 11216–11226; d) K. Mette, A. Bergmann, J. P. Tessonnier, M. Hävecker, L. Yao, T. Ressler, R. Schlögl, P. Strasser, M. Behrens, *ChemCatChem* **2012**, *4*, 851–862.

[32] B. W. Byles, N. K. R. Palapati, A. Subramanian, E. Pomerantseva, *APL Materials* **2016**, *4*, 046108.

[33] a) R. N. De Guzman, A. Awaluddin, Y. F. Shen, Z. R. Tian, S. L. Suib, S. Ching, C. L. O'Young, *Chem. Mater.* **1995**, *7*, 1286–1292; b) S. L. Suib, *Acc. Chem. Res.* **2008**, *41*, 479–487.

[34] a) I. M. Mosa, S. Biswas, A. M. El-Sawy, V. Botu, C. Guild, W. Song, R. Ramprasad, J. F. Rusling, S. L. Suib, *J. Mater. Chem. A* **2016**, *4*, 620–631; b) H. Zheng, M. Modibedi, M. Mathe, K. Ozoemena, *Mater. Today: Proc.* **2017**, *4*, 11624–11629; c) A. M. El-Sawy, C. K. King'ondu, C.-H. Kuo, D. A. Kriz, C. J. Guild, Y. Meng, S. J. Frueh, S. Dharmarathna, S. N. Ehrlich, S. L. Suib, *Chem. Mater.* **2014**, *26*, 5752–5760.

[35] S. Bodoardo, J. Brenet, M. Maja, P. Spinelli, *Electrochim. Acta* **1994**, *39*, 1999–2004.

[36] H. Ma, J. Shen, M. Shi, B. Yan, N. Li, M. Ye, *Mater. Res. Bull.* **2011**, *46*, 1461–1466.

[37] H. M. Rietveld, *Acta Crystallogr.* **1967**, *22*, 151–152.

[38] a) C. C. L. McCrory, S. Jung, J. C. Peters, T. F. Jaramillo, *J. Am. Chem. Soc.* **2013**, *135*, 16977–16987; b) I. Spanos, A. A. Auer, S. Neugebauer, X. Deng, H. Tüysüz, R. Schlögl, *ACS Catalysis* **2017**, *7*, 3768–3778.

[39] J. Vicat, E. Fanchon, P. Strobel, D. Tran Qui, *Acta Crystallogr. Section B* **1986**, *42*, 162–167.

[40] T. Bredow, A. R. Gerson, *Phys. Rev. B* **2000**, *61*, 5194–5201.

[41] T. Homann, U. Hotje, M. Binnewies, A. Börger, K. D. Becker, T. Bredow, *Solid State Sci.* **2006**, *8*, 44–49.

[42] R. Dovesi, A. Erba, R. Orlando, C. M. Zicovich-Wilson, B. Civalleri, L. Maschio, M. Rérat, S. Casassa, J. Baima, S. Salustro, B. Kirtman, *Wiley Interdisciplinary Rev. Comput. Mol. Sci.* **2018**, *8*, e1360.

[43] D. Vilela Oliveira, J. Laun, M. F. Peintinger, T. Bredow, *J. Comput. Chem.* **2019**, *40*, 2364–2376.